

Quantum-assisted learning of graphical models with arbitrary pairwise connectivity

Marcello Benedetti

*Quantum Artificial Intelligence Lab., NASA Ames Research Center, Moffett Field, CA 94035, USA and
Department of Computer Science, University College London, WC1E 6BT London, United Kingdom*

John Realpe-Gómez

*Quantum Artificial Intelligence Lab., NASA Ames Research Center, Moffett Field, CA 94035, USA
SGT Inc., 7701 Greenbelt Rd., Suite 400, Greenbelt, MD 20770, USA and
Instituto de Matemáticas Aplicadas, Universidad de Cartagena, Bolívar 130001, Colombia*

Rupak Biswas

Exploration Technology Directorate, NASA Ames Research Center, Moffett Field, CA 94035, USA

Alejandro Perdomo-Ortiz*

*Quantum Artificial Intelligence Lab., NASA Ames Research Center, Moffett Field, CA 94035, USA and
USRA Research Institute for Advanced Computer Science (RIACS), 615 National, Mountain View CA 94043, USA*

Mainstream machine learning techniques such as deep learning and probabilistic programming rely heavily on sampling from generally intractable probability distributions. There is increasing interest in the potential advantages of using quantum computing technologies as sampling engines to speedup these tasks. However, some pressing challenges in state-of-the-art quantum annealers have to be overcome before we can assess their actual performance. Most notably, the effective temperature at which samples are generated is instance-dependent and unknown, the interaction graph is sparse, the parameters are noisy, and the dynamic range of the parameters is finite. Of all these limitations, the sparse connectivity resulting from the local interaction between quantum bits in physical hardware implementations, is considered the most severe limitation to the quality of constructing powerful machine learning models. Here we show how to surpass this *curse of limited connectivity* bottleneck and illustrate our findings by training probabilistic generative models with arbitrary pairwise connectivity. Our model can be trained in quantum hardware without full knowledge of the effective parameters specifying the corresponding Boltzmann-like distribution. Therefore, inference of the effective temperature is avoided and the effect of noise in the parameters is mitigated. We illustrate our findings by successfully training hardware-embedded models with all-to-all connectivity on a real dataset of handwritten digits and two synthetic datasets. In each of these datasets we show the generative capabilities of the models learned with the assistance of the quantum annealer in experiments with up to 940 quantum bits. Additionally, we show a visual Turing test with handwritten digit data, where the machine generating the digits is a quantum processor. Such digits, with a remarkable similarity to those generated by humans, are extracted from the experiments with 940 quantum bits.

I. INTRODUCTION

Sampling from high-dimensional probability distributions is at the core of a wide spectrum of machine learning techniques with important applications across science, engineering, and society; deep learning [1] and probabilistic programming [2] are some notable examples. While much of the record-breaking performance of machine-learning algorithms regularly reported in the literature pertains to task-specific supervised learning algorithms [1, 3], the development of the more human-like unsupervised learning algorithms has been lagging behind. An approach to unsupervised learning is to model the joint probability distribution of all the variables of interest. This is known as the generative approach because it allows to generate synthetic data by sampling

from the joint distribution. Generative models open up new possibilities and applications in anomaly detection, noise reduction, handling of missing values, visual arts, to name a few. Even in some supervised contexts, it may be useful to treat the targets as standard input and attempt to model the joint distribution. Generative models rely on a sampling engine that is used for both inference and learning. Due to the intractability of traditional sampling techniques like Markov Chain Monte Carlo (MCMC), learning good generative models is among the hardest problems in machine learning [1, 3–6].

Recently, there has been increasing interest in the potential that quantum computing technologies have for speeding up sampling [7–22]. This goes beyond the original focus of the quantum annealing computational paradigm [23–25], which was solving discrete optimization problems [26–33]. Empirical results suggest that under certain conditions quantum annealing hardware samples from a Boltzmann distribution [7, 8, 21, 34, 35]. In principle, the user could adjust the control parameters so

*Electronic address: alejandro.perdomoortiz@nasa.gov

that the device implements the desired Boltzmann distribution. In practice, there exist device-dependent limitations that complicate this process. The most pressing ones are [7, 8, 10, 11, 14]: (i) the effective temperature is parameter-dependent and unknown; (ii) the interaction graph is sparse; (iii) the parameters are noisy; (iv) the dynamic range of the parameters is finite. All these issues need to be overcome before we can assess whether or not quantum annealers can indeed sample more efficiently than traditional techniques on conventional computers.

A relatively simple technique for the estimation of parameter-dependent effective temperature was developed in Ref. [7] and shown to perform well for training restricted Boltzmann machines. More recently, generalizations and alternative techniques have been introduced in Ref. [8]. In the context of Boltzmann machine learning, these techniques need to estimate temperature at each iteration, implying a computational overhead.

Here we put forward an approach that completely sidesteps limitation (i), i.e. the need of estimating temperature at each iteration of the learning process. Furthermore, inspired by fully connected Boltzmann machines, we propose a graphical model embedded in hardware that implements all pairwise interactions between logical variables, substantially improving on limitation (ii). Since the essential components for estimating the gradient needed in the learning process take place on quantum hardware, our approach is more robust to the noise in the parameters improving also on limitation (iii).

Our work here is based on a maximum entropy model, a Boltzmann machine with no hidden variables, whose learning is usually known as the inverse Ising problem [36, 37]. We show that the resulting models embedded in quantum hardware can model well both the real dataset optical recognition of handwritten digits (OptDigits) [38] and the synthetic dataset bars and stripes (BAS) [39]. Moreover, using a dataset of configurations extracted from random instances of the Sherrington-Kirkpatrick model [40–42], we show that our model’s generative performance improves with training and converges to the ideal value.

We emphasize that the objective of this work is not to address the question of quantum speedup in sampling applications, but rather we focus in fixing the most pressing challenges that state-of-the-art quantum annealers face to work properly as sampling engines. We think that the approach in this work is suitable for addressing such a relevant question in the near future, but since benchmarking quantum annealers for machine learning application is a time consuming task, we leave this for a future publication.

The outline of this article is as follows. In Sec. II we introduce the probabilistic model, naturally embedded in quantum hardware and with effective all-to-all connectivity, that we will use in the rest of the work. In Sec. III we derive a learning algorithm suitable for the probabilistic model introduced in Sec. II. In Sec. IV we discuss the implementation details. In Sec. V we describe the ex-

periments performed in two synthetic datasets and a real dataset; we show that the model introduced here trained by using the D-Wave 2X (DW2X) hosted at NASA Ames Research Center displays good generative properties, and can reconstruct and classify data with good accuracy. In Sec. VI we report the conclusions of our work.

II. HARDWARE-EMBEDDED MODELS

A. General considerations

To address the curse of limited connectivity in hardware realizations of quantum annealing, we first define the general setting and then present a probabilistic graphical model that effectively implements an all-to-all pairwise connectivity in quantum hardware. The ideas can be easily extended to arbitrary topologies.

Consider a Boltzmann probability distribution over a vector of binary variables $\mathbf{s} \in \{-1, +1\}^N$

$$P(\mathbf{s}) = \frac{e^{-\beta E(\mathbf{s})}}{Z(\beta)}, \quad (1)$$

where,

$$E(\mathbf{s}) = - \sum_{(i,j) \in \mathcal{E}} J_{ij} s_i s_j - \sum_{i \in \mathcal{V}} h_i s_i \quad (2)$$

is the corresponding energy function, J_{ij} and h_i are real-valued parameters, β is the inverse temperature and $Z(\beta) = \sum_{\mathbf{s}} e^{-\beta E(\mathbf{s})}$ is the normalization constant or partition function. The energy function is defined on an interaction graph $\mathcal{G} = (\mathcal{V}, \mathcal{E})$ where \mathcal{V} and \mathcal{E} are the set of vertices and edges, respectively.

In *combinatorial optimization*, one seeks the configuration of these *binary variables* associated with the lowest energy in Eq. (2). The typical strategy to embed dense graphs in quantum hardware is to represent logical binary variables by subgraphs of the interaction graph of physical qubits. The value of the (ferromagnetic) interactions among qubits in these subgraphs should be fine-tuned such that the ground state of the original problem is preserved and therefore still favored in the physical implementation of the quantum annealing algorithm; this is known as the parameter setting problem (e.g. see Refs. [32, 43]). In *probabilistic modeling*, the scenario is different. When learning a probabilistic model such as the one in Eq. (1), one seeks the configuration of *parameters* J_{ij} and h_i that maximizes a suitable function of the data set.

Notice that in combinatorial optimization problems it is desirable to have the optimal configuration or ground state with probability close to one. When dealing with probabilistic models, however, all configurations matter, along with their corresponding probabilities. By mapping the original problem to quantum hardware, as routinely done in combinatorial optimization applications,

we may end up implementing a Boltzmann distribution that differs from the one defined over logical variables. An additional complication is that finding optimal parameters for a physical device is hampered by lack of precision, noise, and having to infer an instance-dependent effective temperature at each step of the learning.

To avoid computing the instance-dependent effective temperature and mitigate the effects of persistent biases [44], lack of precision, and noise in the control parameters, we take a gray-box model approach. That is, we assume the probability distribution that describes the samples generated by the quantum annealer is like the one in Eq. (1), but we do not need complete knowledge of the actual parameters being implemented. This leads to the condition that the first- and second-order moments of the model and data distributions should be equal for the parameters to be optimal. The assumption that the model is Boltzmann is reflected in the fact that the second moment between particles i and j only influences the update of coupling J_{ij} , and if such a second moment increases (decreases) so does J_{ij} ; still, it leaves open the possibility for the model to effectively self-correct for persistent biases, noise, and lack of precision as long as the estimated gradient has a positive projection on the right direction in the spirit of simultaneous perturbation stochastic approximation [11, 45]. The resulting model is nevertheless tied to the specific machine being used.

To do this, we start from a generic probabilistic model P , like the one in Eq. (1), and build a new probabilistic model \tilde{P} embedded in quantum hardware with effectively the same topology, due to the minor-embedding procedure. More precisely, to each variable s_i of the original probabilistic model we associate a subgraph of the hardware interaction graph. The additional couplings inside a subgraph are part of the hardware-embedded probabilistic model \tilde{P} and have to be learned along with the remaining model parameters that couple different subgraphs. In this way, we leave the fine-tuning of these intra-subgraph couplings to the learning algorithm which has now the potential to learn corrections to the noise affecting the physical components, under the assumption that these defects still respect the direction of the log-likelihood gradient guiding the learning.

In the following, we will focus on hardware-embedded probabilistic models with effective all-to-all connectivity as that is the most general case. Therefore, our derivations and the model proposed here includes any topology with pairwise connectivity.

B. Fully connected inspired models

Formally, we define an energy function over qubits $\mathbf{z} \in \{-1, +1\}^M$ by

$$\tilde{E}(\mathbf{z}) = -\frac{1}{2} \sum_{i,j=1}^N \sum_{k,l=1}^{Q_i, Q_j} J_{ij}^{(kl)} z_i^{(k)} z_j^{(l)} - \sum_{i=1}^N \sum_{k=1}^{Q_i} h_i^{(k)} z_i^{(k)}, \quad (3)$$

where N is the number of logical variables, which equals the number of subgraphs realized in hardware, Q_i is the number of qubits in subgraph i , $z_i^{(k)}$ is qubit k of subgraph i , $h_i^{(k)}$ is the local field for qubit k of subgraph i , and $J_{ij}^{(kl)}$ is the coupling between qubit k of subgraph i and qubit l of subgraph j —when $i = j$, it specifies the interactions within the subgraph, while when $i \neq j$, it specifies the interactions among subgraphs; $J_{ij}^{(kl)} = 0$ if there is no available interaction between the corresponding qubits in the quantum hardware.

Since the number of physical variables $M = \sum_{i=1}^N Q_i$ can be much larger than the number of logical variables N , we need to define two mappings: $\mathbf{z} = f(\mathbf{s})$ from the data space to the qubit space and $\mathbf{s} = g(\mathbf{z})$ from the qubit space to the data space. In this work, we choose the map f to replicate the state of each logical variable s_i inside the corresponding subgraph i , i.e.

$$z_i^{(k)} = s_i, \quad \text{for } k = 1, \dots, Q_i, \quad (4)$$

and the map g to assign the state of the majority of physical variables in subgraph i to the corresponding logical variable s_i , i.e.

$$s_i = \text{sign} \left(\sum_{k=1}^{Q_i} z_i^{(k)} \right). \quad (5)$$

The rationale behind this choice is that, ideally, samples from the trained model are expected to have all qubits $z_i^{(k)}$ in a subgraph i having exactly the same state, i.e. $z_i^{(k)} = z_i^{(l)}$ for $k, l = 1, \dots, Q_i$. In this case, we could pick whichever qubit $z_i^{(k)}$ as representative of the logical variable s_i and this choice would be equivalent to the choice in Eq. (5). However, we expect the choice in Eq. (5) to be more robust to the different sources of noise in quantum annealers by exploiting such a redundancy in the spirit of error correction codes [41, 42].

III. LEARNING ALGORITHM

The energy function in Eq. (3) is designed to overcome connectivity limitations of hardware-embedded graphical models. In what follows, we will show that the adaptation of standard learning procedures to the maximum entropy model proposed here works very well even in the presence of unknown hardware noise on couplings $J_{ij}^{(kl)}$ and local fields $h_i^{(k)}$. Moreover, we can learn suitable intra-subgraph couplings at a rate dictated by the contrast of the strength of pairwise correlations in the model and in the data, without the need for hard-coded values. Previous results [46] suggests that the optimal intra-subgraph couplings of an embedding in quantum hardware is related to the critical temperature of the corresponding instance. The impact of the parameter setting problem discussed above is expected to be stronger

in sampling than in optimization since all configurations and their corresponding probabilities play a role in the former, in contrast to the case of combinatorial optimization problems discussed in [46]. Furthermore, along the learning path the system traverses different classes of instances with no pre-determined optimal subgraph couplings. For these reasons, we think that adaptive intra-subgraph couplings are needed to bypass the issues raised above.

Consider a binary data set $\mathcal{D} = \{\mathbf{s}^1, \dots, \mathbf{s}^D\}$ where each data point can be represented as an array of Ising variables, i.e. $\mathbf{s}^d = (s_1^d, \dots, s_N^d)$ with $s_i^d \in \{-1, +1\}$, for $i = 1, \dots, N$. Applying the mapping defined in Eq. (4), one obtains the extended binary data set $\tilde{\mathcal{D}} = \{\mathbf{z}^1, \dots, \mathbf{z}^D\}$ along with the corresponding empirical distribution $\tilde{Q}(\mathbf{z})$. Similarly to other Boltzmann machines, the learning procedure consists in maximizing the average log-likelihood of the data [47]

$$\mathcal{L}_{\text{av}} = \frac{1}{D} \sum_{d=1}^D \log \tilde{P}(\mathbf{z}^d), \quad (6)$$

with respect to the model parameters $J_{ij}^{(kl)}$ and $h_i^{(k)}$. In this particular case, the log-likelihood is smooth and convex [47, 48] in $J_{ij}^{(kl)}$ and $h_i^{(k)}$, and gradient ascend does not get trapped in poor local maxima. The learning rules are given by

$$J_{ij}^{(kl)}(t+1) = J_{ij}^{(kl)}(t) + \eta \frac{\partial \mathcal{L}_{\text{av}}}{\partial J_{ij}^{(kl)}}, \quad (7)$$

$$h_i^{(k)}(t+1) = h_i^{(k)}(t) + \eta \frac{\partial \mathcal{L}_{\text{av}}}{\partial h_i^{(k)}}, \quad (8)$$

where t indicates the iteration and $\eta > 0$ is the learning rate. The gradient of the average log-likelihood function is given by

$$\frac{\partial \mathcal{L}_{\text{av}}}{\partial J_{ij}^{(kl)}} = \langle z_i^{(k)} z_j^{(l)} \rangle_{\mathcal{D}} - \langle z_i^{(k)} z_j^{(l)} \rangle_{\mathcal{M}}, \quad (9)$$

$$\frac{\partial \mathcal{L}_{\text{av}}}{\partial h_i^{(k)}} = \langle z_i^{(k)} \rangle_{\mathcal{D}} - \langle z_i^{(k)} \rangle_{\mathcal{M}}. \quad (10)$$

Here $\langle \cdot \rangle_{\mathcal{D}}$ denotes the ensemble average with respect to the distribution $\tilde{Q}(\mathbf{z})$ that involves only the data and is commonly referred to as the *positive phase*. Similarly, $\langle \cdot \rangle_{\mathcal{M}}$ denotes the ensemble average with respect to the distribution $\tilde{P}(\mathbf{z})$ that involves exclusively the model and has been named the *negative phase*.

The exact computation of model's statistics is a computational bottleneck due to the intractability of computing the partition function and the exponential number of terms in the configuration space. An efficient approximation of the statistics is therefore required and it is usually carried out by standard sampling techniques such as MCMC. In this work we instead rely on the working assumption that quantum annealers can generate samples

from a Boltzmann distribution. According to our results to be presented below, this seems to be a reasonable assumption.

The learning procedure implemented by Eqs. (9) and (10) can be interpreted as entropy maximization under constraints on the first and second-order moments [36, 48–50]. In Ref. [20], the maximum entropy approach was implemented on a D-Wave device in the context of information decoding, which is a hard optimization problem. Instead, we use maximum entropy inference for a hard machine learning task, i.e., in unsupervised learning of generative models.

A few remarks are in order: (i) the actual shape of a Boltzmann distribution is characterized by $\beta J_{ij}^{(kl)}$ and $\beta h_i^{(k)}$. Multiplying Eqs. (7) and (8) by β we observe that the actual learning is taking place at a learning rate $\beta\eta$ that can vary since the effective temperature is instance-dependent [7]; (ii) Eq. (7) implies that the intra-subgraph couplings $J_{ii}^{(kl)}$ always increases at a varying rate proportional to $1 - \langle z_i^{(k)} z_i^{(l)} \rangle$; (iii) the problem of estimating the parameters of an Ising model is usually called the inverse Ising problem [36, 37, 51], and some of the main alternative techniques for its solution are mean field and pseudo-likelihood methods.

IV. IMPLEMENTATION DETAILS

A. Device and embeddings

We run experiments on the DW2X quantum annealer located at NASA Ames Research Center. The device is equipped with 1152 qubits interacting according to a graph known as Chimera connectivity. For the DW2X device hosted at NASA Ames, only 1097 qubits are functional and available to be used. Assuming all 1152 qubits were available, the schema for minor embedding described in Ref. [46] would allow us to embed a fully connected graph with up to 48 logical variables. Since only 1097 qubits are available, such schema cannot be used and the size of the largest fully connected model that can be implemented is reduced. The problem of finding the best minor embedding in terms of the smallest number of qubits needed to represent the original logical graph, is an NP-hard problem itself. For the embeddings of the instances studied here, we run the `find_embedding` heuristic [52] offered by D-Wave's API and use the best embedding found within the 500 requested trials. We judged the quality of an embedding not only by the total number of physical qubits needed to represent the logical graph, but also considering and preferring smaller maximum subgraph size for the logical units. For example, in the case of the 46-variable fully connected graph, we found an embedding with 917 qubits and a maximum subgraph size of 34. As shown in Table I, we selected instead an embedding with a larger number of qubits,

940, but with a considerably smaller maximum subgraph size of 28. Table I shows details for each of the embeddings used in our experiments. Figure 6 shows the physical connectivity of the 46-variable embedding where each subgraph is represented by a number and a color. Finally, the parameter range allowed by DW2X is $J_{ij}^{(kl)} \in [-1, +1]$ and $h_i^{(k)} \in [-2, +2]$.

n_{logical}	n_{physical}	Min	Max	Chip usage
20	128	5	8	12%
42	739	11	25	67%
46	940	12	28	86%

TABLE I: Main characteristics of the different embeddings used here, for each of the fully connected graphs with a number of logical variables n_{logical} , embedded into a number of physical qubits n_{physical} . All embeddings were generated by the heuristic called `find_embedding` [52] provided by D-Wave’s API. The table includes information about the minimum (Min) and maximum (Max) subgraph size and the percentage of used qubits relative to those available (Chip usage).

B. Data sets and preprocessing

We tested our ideas on both the real dataset optical recognition of handwritten digits (OptDigits) [38] and the synthetic dataset bars and stripes (BAS) [39].

The OptDigits dataset required the preprocessing steps shown in Fig. 1. Firstly, each picture is 8×8 and has a categorical variable indicating the class it is belonging to. Using standard one-hot encoding for the class (i.e. $c_i^d = -1$ for $i \neq j$, $c_j^d = +1$ where j indexes the class for picture d), we would need to embed a fully connected graph of 74 variables, 64 for the pixels and 10 for the class, exceeding what we can embed in the DW2X. We removed the leftmost and rightmost columns as well as the bottom row from each picture reducing the size to 7×6 and retaining the readability. Secondly, we selected only four classes of pictures, those corresponding to digits “one” to “four” reducing the one-hot encoding to four variables. The four classes account for 1545 pictures in the training set and 723 pictures in the test set, and they are in almost equal proportion in both. Finally, the original 4-bit grayscale of each pixel is thresholded at the midpoint and binarized to $\{-1, +1\}$ in order for the data to be represented by qubits in the DW2X. Figure 2 (a) shows some pictures from the test set.

The BAS dataset consists of $N \times M$ pictures generated by setting the pixels of each row (or column) to either black (-1) or white ($+1$), at random. A reason to use this synthetic dataset is that it can be adapted to the number of available variables in the DW2X. Having found an embedding for the 42-variable fully connected graph, we generated a 7×6 BAS dataset consisting of 192 pictures of 42 binary variables each. Then, we randomly shuffled the pictures and split the dataset into training

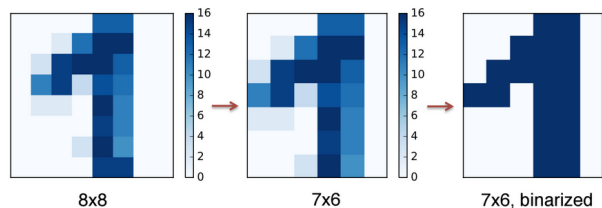


FIG. 1: *OptDigits preprocessing steps*: the original 8×8 pictures are cropped to 7×6 arrays by removing columns from the left and the right, as well as deleting a row from the bottom. Finally, the 4-bit grayscale is thresholded at the midpoint and binarized to $\{-1, +1\}$. Figure 2 (a) shows some pictures from the test set.

and test sets of size 96 each. Figure 3 (a) shows some pictures from the test set.

C. Choice of hyperparameters

We distinguish two kinds of hyperparameter: those associated with the device and those referring to the gradient. Device hyperparameters affect the time needed to obtain samples. We set them to their corresponding minimum values in order to obtain samples as fast as possible. Gradient hyperparameters come from advanced techniques known to improve generalization and speeding up learning. We adopted standard $L2$ regularization for the pairwise interactions, and momentum for all the parameters, hence introducing two hyperparameters in Eqs. (7) and (8) (see Ref. [53] for discussion about implementation details and best practices). For these, we tried a small grid of values and chose the value that would allow the quantum-assisted algorithm to produce visually appealing samples. All the experiments were performed using the hyperparameters shown in Tab. II.

Domain	Hyperparameter	Value
device	annealing time	$5\mu s$
	programming thermalization	$1\mu s$
	readout thermalization	$1\mu s$
	auto scale	False
gradient	learning rate	0.0025
	$L2$ regularization	10^{-5}
	momentum	0.5

TABLE II: Settings used in all the experiments

V. RESULTS

A. Reconstruction of pictures

The first task we address is verifying that the model is indeed able to learn the joint probability distribution of variables given a data set. One way to do this is to

check whether the learned model can reconstruct corrupted pictures. To generate a reconstruction, each *correct* pixel can be clamped by applying strong local fields to all qubits of the corresponding subgraphs. We then generated samples from the learned model and assigned values to each *corrupted* pixel s_i using the majority vote map (Eq. (5)) for all qubits in the corresponding subgraph i . To further mitigate the noise associated to this, we generated multiple reconstructions, 100 for each corrupted picture, and took a second majority vote over them. We chose to interrupt the training of the models as soon as any of the parameters went out of the dynamic range of the device. Since the intra-subgraph couplings always increase, we expect these to be the first to get out of range and we observed so in the experiments described below. We do this here with two datasets, OptDigits and BAS.

1. Optical recognition of handwritten digits

We trained a model on the real dataset OptDigits, a sample of which is shown in Fig. 2 (a). Since the training set contains a relatively large number of data points, we opted for a mini-batch learning approach [53], where 200 data points were used at each iteration to compute the positive phase of the gradient. The negative phase is computed on 200 samples from DW2X. We trained for 6000 iterations after which an intra-subgraph coupling went outside the dynamic range of the device.

To evaluate the model, we added a 50% uniformly distributed “salt-and-pepper” noise (Fig. 2 (b), red pixels) to each picture of the test set and used the model to reconstruct it. Notice that, given a corrupted picture, it is not always possible to obtain perfect reconstruction as multiple solutions could be correct. Therefore, we do not compute any error measure, but rather visually inspect the reconstructions. Fig. 2 (c),(d),(e) and (f) show some reconstructions obtained by models learned after 1, 100, 1000 and 6000 iterations respectively. We can observe that qualitatively good reconstructions are already available from early stages of training. However, the large degree of corruption in the original image gives rise to things such as thicker reconstructions (Fig. 2 (f), 3rd row, 4th column), thinner reconstructions (Fig. 2 (e), 4th row, 2nd column), change of digit “three” into “one” (Fig. 2 (e), 3rd row, 5th column), among others.

2. Bars and stripes

We performed a similar test on the 7×6 BAS, a sample of which is shown in Fig. 3 (a). We computed the positive phase once using all the 96 data points. Then, we ran the learning procedure and for each iteration we computed the negative phase out of 96 samples obtained from the DW2X. The learning process stopped at iter-

ation 3850 after which an intra-subgraph coupling exceeded the maximum value allowed.

To evaluate the model, we blacked-out a 5×4 block (Fig. 3 (b), red pixels corresponding to 47.6% of the image) from each picture of the test set and use the model to reconstruct it. We can observe from Fig. 3 (e) that reconstructed pictures are qualitatively similar to the original ones. To have a quantitative estimate of the quality of the reconstruction, we computed the expected number of incorrect pixel values (or mistakes) per reconstruction. After one iteration (Fig. 3 (c)) we obtained a rate of 10.45 mistakes out of 20 corrupted pixels, corresponding to about 50% performance as expected. The number of mistakes decreased to 3.73 (18.6%) after 100 iterations (Fig. 3 (d)), 0.59 (2.95%) after 1000 (Fig. 3 (f)), and finally 0.13 (0.65%) at the end of training (Fig. 3 (e)). The latter result corresponds to almost perfect reconstruction. Notice that no picture from the test set was ever input to the model during training. Hence, these results provide evidence that the joint probability distribution of the pixels has been correctly modeled and we can most likely rule out a simple memorization of the patterns.

B. Generation and classification of pictures

To investigate the generative and classification capabilities of the model, we introduced a one-hot encoding of the four classes of the OptDigits dataset, therefore introducing 4 additional logical variables, for a total of 46. We trained this larger model on the OptDigits dataset including also the classes.

We performed a simple classification task that does not require turning the generative model into a discriminative one by additional post-training. We classify each test picture as $c^* = \arg \max_c P(\mathbf{c}|\mathbf{s})$, where \mathbf{s} is the vector encoding the pixels and \mathbf{c} is the vector encoding the classes. To approximate the probability, we clamped the subgraphs, by applying strong local fields, to the pixel values corresponding to the picture to be classified and sampled the four class variables from DW2X. We generated 100 samples for each picture and assigned the picture to the most frequent class. This simple procedure led to an accuracy of 90% on the 723 test pictures. This is a significant result, given that a random guess achieves 25% accuracy. However, it is to be expected that a fine-tuned discriminative model can achieve better accuracy.

Finally, Figure 4 shows samples obtained from the DW2X by first setting the class variables, by applying strong local fields, to classes “one” to “four” (one class per column), along with human-generated pictures from the test set. Rows correspond to either human-generated pictures from the test set or to machine-generated pictures. We defer the answer to this visual Turing test to a footnote [56]. Machine-generated pictures are remarkably similar, though not identical, to those drawn by humans. Notice that human-generated digits may be

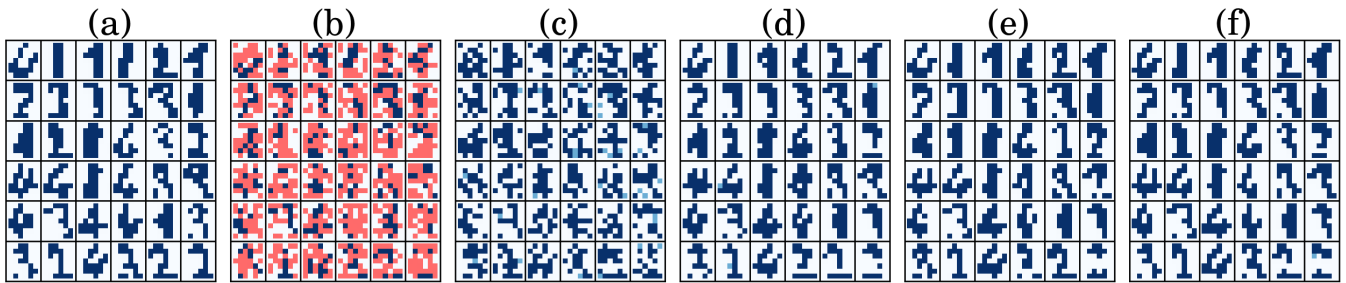


FIG. 2: *OptDigits experiment*: (a) 36 samples from the test set with each pixel being either dark blue (+1) or white (-1). See Fig. 1 and the main text for a description of the preprocessing steps. (b) A uniform “salt-and-pepper” noise shown in red corrupts each picture. The model cannot use information from the red area. (c) (d) (e) (f) Reconstructions obtained after 1, 10, 1000 and 6000 learning iterations. A light blue pixel indicates a tie of the majority vote over the corresponding subgraph. We can visually verify that the model has learned to generate digits. The learning stops at iteration 6000 because further iterations would bring some parameters out of the dynamic range of the DW2X device.

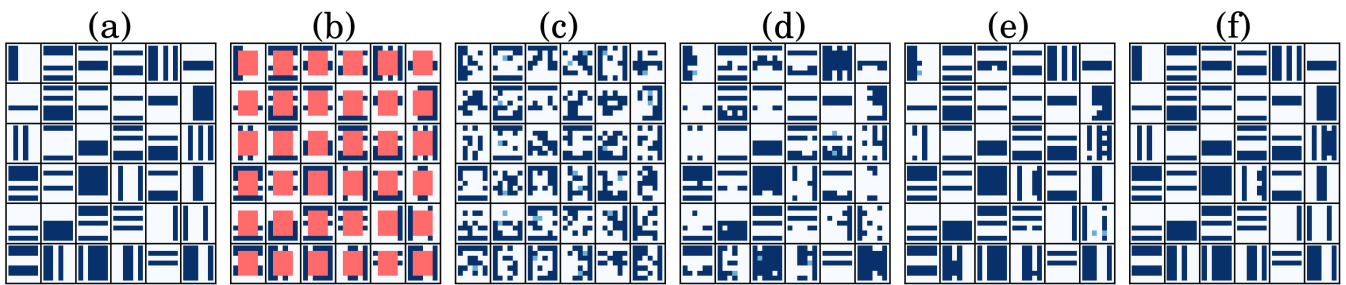


FIG. 3: *BAS experiment*: (a) (a) 36 samples from the test set with each pixel being either dark blue (+1) or white (-1). (b) A 5×4 block of noise shown in red corrupts each picture. The model cannot use information from the red area and yet the remaining pixels contain enough information to reconstruct the original picture. (c) (d) (e) (f) Reconstructions obtained after 1, 10, 1000 and 3850 learning iterations. The average number of mistaken pixels is 50% in (c), 18.6% in (d), 2.95% in (e) and finally 0.65% in (f). This is an almost perfect reconstruction. The learning stops at iteration 3850 because further iterations would bring some parameters out of the dynamical range of the DW2X device.

ambiguous because of the variety of calligraphy styles and the low resolution of the pictures in the dataset. This characteristic has been retained in the machine-generated pictures. This characteristic has been retained in the machine-generated pictures.

C. Learning of an Ising model

In the previous section we showed that the hardware-embedded model introduced here can be successfully trained by our quantum-assisted learning algorithm on both real-world pictures and synthetic datasets, and can also be used for reconstruction and classification tasks. Here we compare the physical model trained from samples generated by quantum annealing and the logical model trained by samples generated by simulated thermal annealing [54]. To simplify this task, we now deal with datasets generated exhaustively from small-sized Boltzmann distributions associated to an Ising model with given parameters, i.e. Eqs. (1) and (2). This is more similar in spirit to the approach usually taken in the literature on the inverse Ising problem [36, 37]. We however

do not quantify the quality of the trained model by the quadratic error between the parameters of the original model and those obtained by the learning algorithms, as it is usually done, for three reasons: i) in our gray-box model approach we do not have access to the effective parameters implemented in the quantum annealer; ii) the physical model has a larger number of parameters than the logical model; iii) to our knowledge there is no direct connection between distances in parameter space, as measured by the quadratic error, and distances in probability space, which are those that have actual operational meaning. To measure distances in parameter space that correspond to distances in probability space it is necessary to use the Fisher information metric. It is known, for instance, that close to a critical point a slight variation in the parameters can lead to drastically different probability distributions [55].

The strategy we take for evaluating the model is as follows: We first set the parameters to implement a desired Boltzmann distribution $Q(\mathbf{s})$. For the size $N = 20$ of the fully connected model considered here, we can exhaustively compute probabilities for all the binary configurations. This allows us to sample from the inverse cumula-

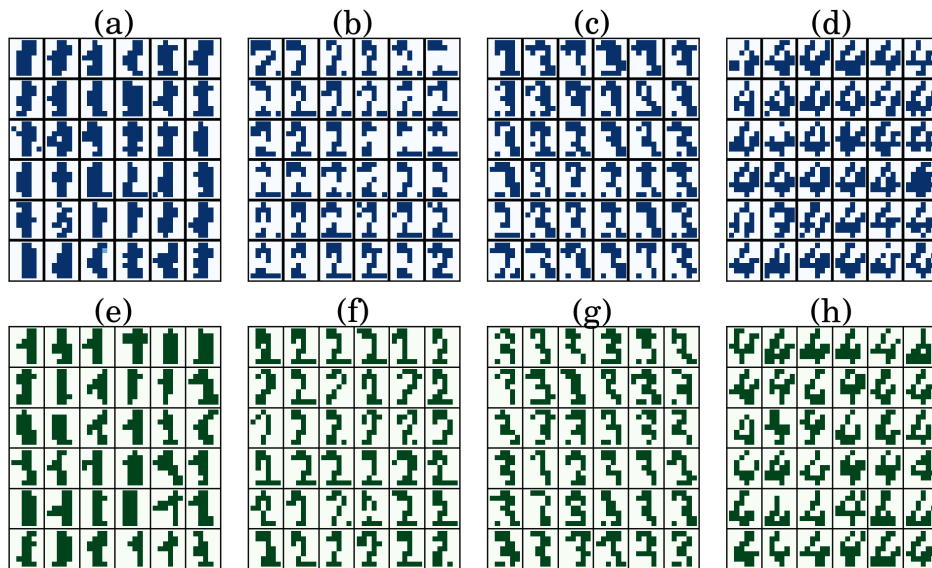


FIG. 4: *Visual Turing test*: the reader is invited to distinguish between human-generated pictures from the test set and machine-generated pictures sampled from the model. Columns identify classes “one” to “four”, rows identify the source “human” or “machine”. The solution is given in a footnote [56].

tive distribution and generate a dataset $\mathcal{D} = \{\mathbf{s}^1, \dots, \mathbf{s}^D\}$ composed of D samples of the desired Boltzmann distribution. We then train models on such a dataset using either quantum annealing on the physical graph or simulated thermal annealing on the logical graph. At each iteration, or epoch, we generate a set $\mathcal{S} = \{\mathbf{s}^{(1)}, \dots, \mathbf{s}^{(L)}\}$ of L samples from the trained models and evaluate the average log-likelihood that such samples were generated by the original model

$$\begin{aligned} \Lambda_{\text{av}}(\mathcal{S}) &= \frac{1}{L} \sum_{\ell=1}^L \log Q(\mathbf{s}^{(\ell)}) \\ &= -\beta \frac{1}{L} \sum_{\ell=1}^L E(\mathbf{s}^{(\ell)}) - \log Z(\beta); \end{aligned} \quad (11)$$

for simplicity we choose $L = D$.

Notice the substantial difference between Eqs. (6) and (11): the former requires full knowledge of the parameters of the models being trained, while the latter requires full knowledge of the distribution that generated the data. Clearly, this approach is unfeasible for real datasets since the whole point of learning a model is precisely that we do not know the true distribution that generated the data. We have also preferred to work with small sized instances in order to have a more clear assessment by relying on exhaustive computations. However, notice that this proxy is more related to the generalization properties of the trained models since it corresponds to the likelihood that new arbitrary samples generated by the trained models were actually generated by the original model. We expect this to be a faithful metric since achieving good generalization performance is the main objective of machine learning techniques. We should take

into account, however, that $\Lambda_{\text{av}}(\mathcal{S})$ is not expected to be maximized by the generated samples, but rather to match the value $\Lambda_{\text{av}}(\mathcal{D})$ of the original dataset. Indeed, the left hand side of Eq. (11) takes its maximum value when \mathcal{S} is made up of only ground state configurations.

We chose to work with 10 random instances of a Sherrington-Kirkpatrick model with $N = 20$ logical variables. Parameters J_{ij} were sampled from a Gaussian with mean $\mu = 0$ and standard deviation $\sigma = 1/\sqrt{N}$, while parameters h_i were set to 0. In this setting, the critical temperature is expected to be $T_c = 1$ in the thermodynamic limit, although finite-size corrections are expected to be relevant for this small size. In order to obtain interesting structures within the probability distribution, we chose temperature $T = 0.5$. We generated $D = 200$ samples and verified that the problem was expected to be indeed difficult by checking that the overlap distribution[40, 41] was non-trivial and by checking the performance of the closed-form solutions obtained by mean-field techniques in Ref. [37]. The mean-field method indeed failed to produce (real-valued) solutions in 8 out of the 10 random instances generated, while performed well in the remaining two instances, adding further evidence that these instances had non-trivial features in their energy landscape.

Next, we trained models via quantum annealing on the physical graph (see details in Tab. I) and simulated thermal annealing on the logical graph. In both models we computed the gradient using $D = 200$ samples, the same size of the training set. For simulated annealing we chose a linear schedule as in Ref. [46] and performed 1000 spin updates from $T_{\text{max}} = 10$ to $T_{\text{min}} = 1$. In our implementation, each sample follows its own schedule.

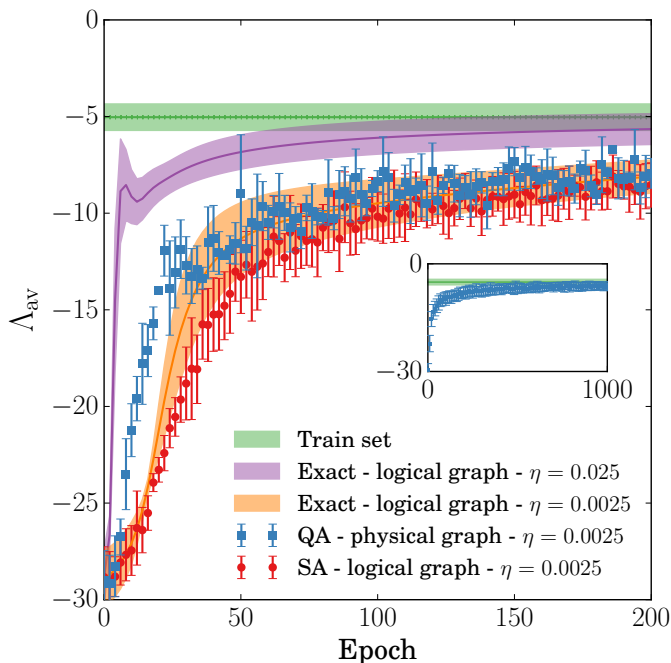


FIG. 5: *Comparison of sampling techniques:* the main plot shows mean and one standard deviation of the proxy Λ_{av} for 10 random instances with $N = 20$ logical variables each for four different learning procedures. A learning procedure is considered successful if it can generalize, that is, if it matches the proxy of the training set (green band). Sampling by quantum annealing on the physical graph (blue squares) enables faster matching than both simulated thermal annealing (red circles) and exact-gradient on the logical graph (orange band). This has been observed in the first 200 learning epochs provided that all methods have the same learning rate $\eta = 0.0025$. However, the exact-gradient procedure equipped with a larger learning rate $\eta = 0.025$ (purple band) outperforms the quantum-assisted algorithm. This empirical results could be explained by the hardware-embedded model having unknown effective temperature acting as a larger learning rate. The inset shows that the quantum-assisted procedure converges to the ideal value of the training set (green band) within 1000 learning epochs.

This procedure better resembles quantum annealing and remove autocorrelation among samples.

Figure 5 shows mean and one standard deviation of the proxy Λ_{av} for 10 random instances and four different learning procedures. The proxy of the model trained via quantum annealing (blue squares) gets close to the ideal value of the training set (green band) at faster pace than that of the model trained by simulated annealing (red circles). To investigate this further, we performed an expensive learning by computing the exact gradient on the logical graph. The figure shows that quantum annealing outperforms the exact-gradient procedure at equal learning rate $\eta = 0.0025$ (orange band). Therefore, the better initial performance associated to quantum annealing cannot be explained solely by the possibility of a sub-optimal setting of the simulated annealing algorithm. We run

exact-gradient with larger learning rate $\eta = 0.025$ (purple band) and found that it does outperform quantum annealing. This indicates that there could be a varying effective learning rate induced by the instance-dependent effective temperature [7, 8] at which a quantum annealer samples. Additionally, performance may also be influenced by the fact that the physical model has a larger number of parameters than the logical model. Further studies of simulated thermal annealing on the physical graph will be needed to address this question.

Finally, we continued to iterate the quantum-assisted procedure and observed convergence to the ideal value of the training set (green band) within 1000 epochs (Figure 5, inset). Hence, the model improves its generative performance with longer training.

We stress that neither the computation of Λ_{av} nor the exact-gradient learning are feasible in real-life applications.

VI. CONCLUSIONS

Whether quantum annealing can improve algorithms that rely on sampling from complex high-dimensional probability distributions is an important open research question. There are, however, several challenges faced by quantum annealers that need to be overcome before we can address such a question from an experimental perspective. Besides the problem of proper temperature estimation which has been addressed recently [7, 8], some of the most pressing challenges are limited connectivity and size of the models that can be implemented, low-precision and limited range of the control parameters, as well as different sources of noise that affect the performance of state-of-the-art quantum annealers [14].

The approach introduced here substantially improves over connectivity limitations. By working on a gray-box model framework, which requires only partial information about the actual distribution the quantum annealer is sampling from, this approach also avoids the need of estimating temperature during the learning of the models and has the potential to help mitigate the different sources of noise on the device. The resulting model can be interpreted as a visible-only Boltzmann machine with all pairwise interactions among logical variables. We validated our ideas qualitatively by training the fully connected hardware-embedded model for reconstruction and generation of pictures, and quantitatively by computing a proxy on datasets extracted from randomly generated Boltzmann distributions.

Natural extensions of the model will be inclusion of latent variables, also known as hidden units, and support for continuous variables. Hidden units are needed, for example, if visible patterns require constraints that cannot be enforced by pairwise interactions alone [47]. Continuous variables are needed for a correct modeling of real datasets.

From a more fundamental perspective, several key

questions remain open: When and why could we expect the quantum annealer to do better than classical MCMC approaches? Our results show that the quantum-assisted learning algorithm is having a faster learning rate during the initial stage, in the scenario where both classical (exact gradient estimation and SA) and our hybrid quantum-classical approach are set under the same conditions in terms of hyperparameters. Given that an instance-dependent effective temperature can imply a varying learning rate, this faster learning is probably due to the quantum-assisted algorithm automatically adjusting its learning rate. In this respect, it is important to investigate if such learning schedule is optimal, and if so whether it can be efficiently simulated by classical means. Still, we cannot discard at this point that some non-trivial quantum effects are playing a role here.

Arguably, this question of whether or not there is quantum speedup in sampling applications is the most important question propelling our research and a potential breakthrough in quantum machine learning research. Years of experience accumulated with the use of quantum annealers for combinatorial optimization suggest that the answer is not straightforward. Furthermore, benchmarking quantum annealers for sampling applications is expected to be more challenging as we have to deal with the whole distribution of states, not only with the ground state as is the case of combinatorial optimization applications. We expect the approach put forward in this work to provide a suitable framework for addressing such a question.

Acknowledgements

This work was supported in part by the AFRL Information Directorate under grant F4HBKC4162G001, the Office of the Director of National Intelligence (ODNI), and the Intelligence Advanced Research Projects Activity (IARPA), via IAA 145483. The views and conclusions contained herein are those of the authors and should not be interpreted as necessarily representing the official policies or endorsements, either expressed or implied, of ODNI, IARPA, AFRL, or the U.S. Government. The U.S. Government is authorized to reproduce and distribute reprints for Governmental purpose notwithstanding any copyright annotation thereon.

Appendix A: Example: Embedding of a fully connected graph with 46 logical units into 940 physical qubits.

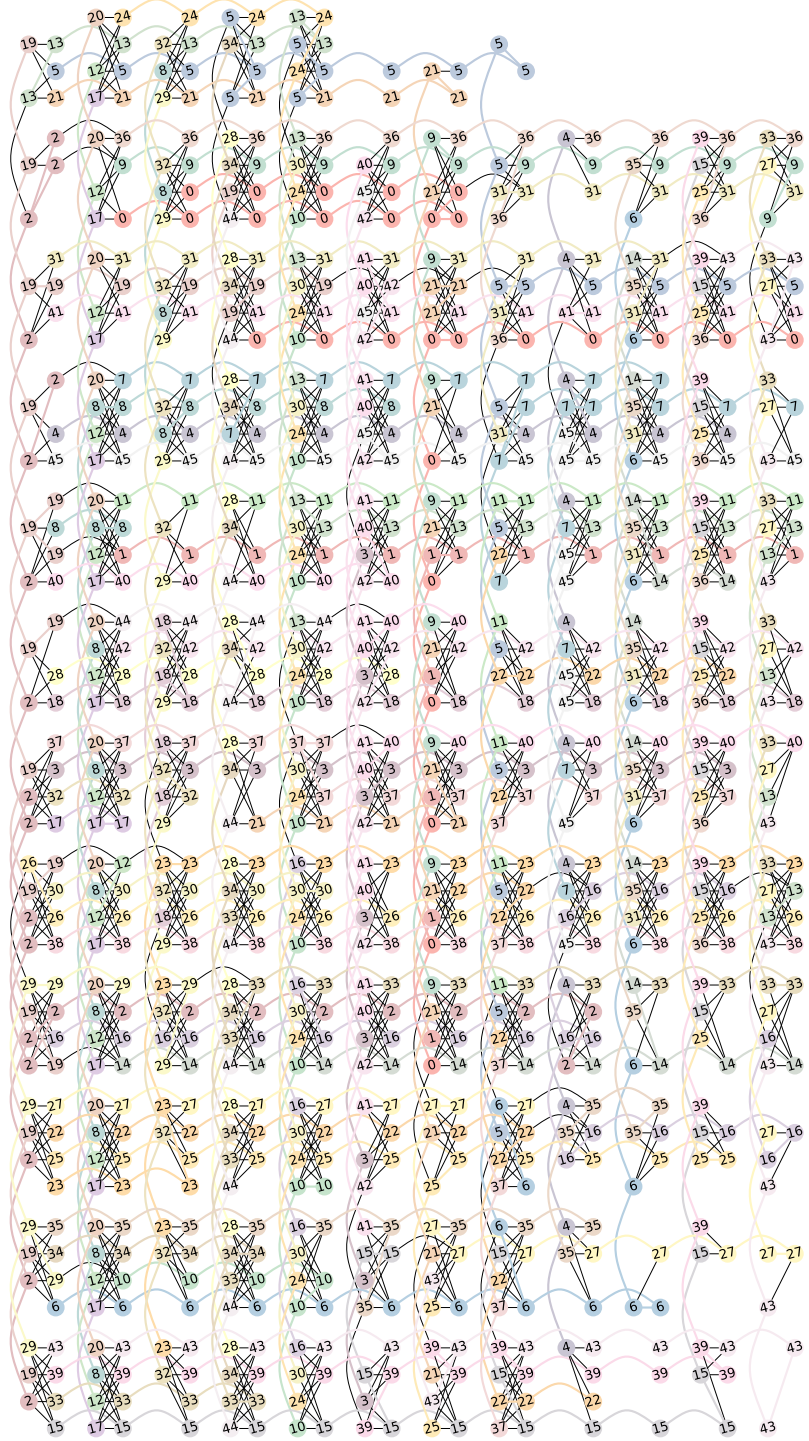


FIG. 6: *Embedding*: 46 logical variables embedded into DW2X's chimera graph using 940 physical variables. Qubits belonging to a logical variable are identified by the same number and linked by edges of the same color. This embedding uses 86% of DW2X's resources.

- [1] Y. LeCun, Y. Bengio, and G. Hinton, *Nature* **521**, 436 (2015).
- [2] Z. Ghahramani, *Nature* **521**, 452 (2015).
- [3] I. G. Y. Bengio and A. Courville (2016), book in preparation for MIT Press, URL <http://www.deeplearningbook.org>.
- [4] R. Salakhutdinov, *Annual Review of Statistics and Its Application* **2**, 361 (2015).
- [5] A. Sinclair and M. Jerrum, *Inf. Comput.* **82**, 93 (1989), ISSN 0890-5401.
- [6] A. Frigessi, F. Martinelli, and J. Stander, *Biometrika* **84**, 1 (1997).
- [7] M. Benedetti, J. Realpe-Gómez, R. Biswas, and A. Perdomo-Ortiz, *Phys. Rev. A* **94**, 022308 (2016).
- [8] J. Raymond, S. Yarkoni, and E. Andriyash, arXiv:1606.00919 (2016).
- [9] H. Neven, V. S. Denchev, M. Drew-Brook, J. Zhang, W. G. Macready, and G. Rose, in *Demonstrations at NIPS-09, 24th Annual Conference on Neural Information Processing Systems* (2009), pp. 1–17.
- [10] Z. Bian, F. Chudak, W. G. Macready, and G. Rose, *Tech. Rep., D-Wave Systems* (2010).
- [11] M. Denil and N. De Freitas, *NIPS Deep Learning and Unsupervised Feature Learning Workshop* (2011).
- [12] S. Lloyd, M. Mohseni, and P. Rebentrost, arXiv:1307.0411 (2013).
- [13] K. Pudenz and D. Lidar, *Quantum Information Processing* **12**, 2027 (2013).
- [14] V. Dumoulin, I. J. Goodfellow, A. C. Courville, and Y. Bengio, in *Proceedings of the Twenty-Eighth AAAI Conference on Artificial Intelligence, July 27 -31, 2014, Québec City, Québec, Canada.* (2014), pp. 1199–1205.
- [15] S. Lloyd, M. Mohseni, and P. Rebentrost, *Nature Physics* **10**, 631 (2014).
- [16] P. Rebentrost, M. Mohseni, and S. Lloyd, *Phys. Rev. Lett.* **113**, 130503 (2014).
- [17] K. M. S. Nathan Wiebe, Ashish Kapoor, arXiv:1412.3489 (2015).
- [18] S. Aaronson, *Nature Physics* **11**, 291 (2015), commentary.
- [19] S. H. Adachi and M. P. Henderson, arXiv:1510.06356 (2015).
- [20] N. Chancellor, S. Szoke, W. Vinci, G. Aeppli, and P. A. Warburton, *Scientific reports* **6** (2016).
- [21] Mohammad H. Amin and Evgeny Andriyash and Jason Rolfe and Bohdan Kulchitsky and Roger Melko, arXiv:1601.02036 (2016).
- [22] J. E. Dorband, in *Information Technology - New Generations (ITNG), 2015 12th International Conference on* (2015), pp. 703–707.
- [23] A. Fennila, M. Gomez, C. Sebenik, C. Stenson, and J. Doll, *Chemical Physics Letters* **219**, 343 (1994).
- [24] T. Kadowaki and H. Nishimori, *Phys. Rev. E.* **58**, 5355 (1998).
- [25] E. Farhi, J. Goldstone, S. Gutmann, J. Lapan, A. Lundgren, and D. Preda, *Science* **292**, 472 (2001).
- [26] F. Gaitan and L. Clark, *Phys. Rev. Lett.* **108**, 010501 (2012).
- [27] A. Perdomo-Ortiz, N. Dickson, M. Drew-Brook, G. Rose, and A. Aspuru-Guzik, *Sci. Rep.* **2**, 571 (2012).
- [28] Z. Bian, F. Chudak, R. Israel, B. Lackey, W. G. Macready, and A. Roy, *Frontiers in Physics* **2** (2014), ISSN 2296-424X.
- [29] B. O’Gorman, R. Babbush, A. Perdomo-Ortiz, A. Aspuru-Guzik, and V. Smelyanskiy, *The European Physical Journal Special Topics* **224**, 163 (2015), ISSN 1951-6355.
- [30] E. G. Rieffel, D. Venturelli, B. O’Gorman, M. B. Do, E. M. Prystay, and V. N. Smelyanskiy, *Quantum Information Processing* **14**, 1 (2015), ISSN 1570-0755.
- [31] Perdomo-Ortiz, A., Fluegemann, J., Narasimhan, S., Biswas, R., and Smelyanskiy, V.N., *Eur. Phys. J. Special Topics* **224**, 131 (2015).
- [32] A. Perdomo-Ortiz, J. Fluegemann, R. Biswas, and V. N. Smelyanskiy, arXiv:1503.01083 (2015).
- [33] D. Venturelli, D. J. Marchand, and G. Rojo, arXiv:1506.08479 (2015).
- [34] M. H. Amin, *Phys. Rev. A* **92**, 052323 (2015).
- [35] M. Benedetti, Master’s thesis, Université Lumière Lyon 2, France (2015).
- [36] E. Schneidman, M. J. Berry, R. Segev, and W. Bialek, *Nature* **440**, 1007 (2006).
- [37] F. Ricci-Tersenghi, *Journal of Statistical Mechanics: Theory and Experiment* **2012**, P08015 (2012).
- [38] M. Lichman, *UCI machine learning repository* (2013), URL <http://archive.ics.uci.edu/ml>.
- [39] D. J. C. MacKay, *Information Theory, Inference & Learning Algorithms* (Cambridge University Press, New York, NY, USA, 2002), ISBN 0521642981.
- [40] M. Mezard, G. Parisi, and M. Virasoro, *Spin Glass Theory and Beyond*, Lecture Notes in Physics Series (World Scientific, 1987), ISBN 9789971501150.
- [41] M. Mezard and A. Montanari, *Information, Physics, and Computation* (Oxford University Press, Inc., New York, NY, USA, 2009), ISBN 019857083X, 9780198570837.
- [42] H. Nishimori, *Statistical Physics of Spin Glasses and Information Processing: An Introduction*, International series of monographs on physics (Oxford University Press, 2001), ISBN 9780198509400.
- [43] V. Choi, *Quantum Information Processing* **7**, 193 (2008).
- [44] A. Perdomo-Ortiz, B. O’Gorman, J. Fluegemann, R. Biswas, and V. N. Smelyanskiy, *Sci. Rep.* **6**, 18628 (2016).
- [45] J. C. Spall, *Introduction to Stochastic Search and Optimization* (John Wiley & Sons, Inc., New York, NY, USA, 2003), 1st ed., ISBN 0471330523.
- [46] D. Venturelli, S. Mandrà, S. Knysh, B. O’Gorman, R. Biswas, and V. Smelyanskiy, *Phys. Rev. X* **5**, 031040 (2015).
- [47] D. H. Ackley, G. E. Hinton, and T. J. Sejnowski, *Cognitive science* **9**, 147 (1985).
- [48] A. L. Berger, V. J. D. Pietra, and S. A. D. Pietra, *Computational linguistics* **22**, 39 (1996).
- [49] E. Jaynes and G. Bretthorst, *Probability Theory: The Logic of Science* (Cambridge University Press, 2003), ISBN 9780521592710.
- [50] E. T. Jaynes, *Phys. Rev.* **106**, 620 (1957).
- [51] M. Mézard and T. Mora, *Journal of Physiology-Paris* **103**, 107 (2009), ISSN 0928-4257, *Neuromathematics of Vision*.
- [52] J. Cai, W. G. Macready, and A. Roy, arXiv:1406.2741 (2014).

- [53] G. E. Hinton, in *Neural Networks: Tricks of the Trade (2nd ed.)*, edited by G. Montavon, G. B. Orr, and K.-R. Müller (Springer, 2012), vol. 7700 of *Lecture Notes in Computer Science*, pp. 599–619, ISBN 978-3-642-35288-1.
- [54] S. Kirkpatrick, C. Gelatt, and M. Vecchi, *Science* **220**, 671 (1983).
- [55] I. Mastromatteo and M. Marsili, *Journal of Statistical Mechanics: Theory and Experiment* **2011**, P10012 (2011).
- [56] Blocks (a) to (d) show machine-generated pictures while blocks (e) to (h) show human-generated pictures. For simplicity, we have not done the standard Turing test, where each pair of figures is shown in isolation. Ours is a harder test for the machine as the redundancy of having all human- and machine-generated images together enhances the probability of a human to spot differences between the two types of images.